



OPEN

SUBJECT AREAS:  
BATTERIES  
ELECTROCHEMISTRYReceived  
27 August 2014Accepted  
4 November 2014Published  
25 November 2014Correspondence and  
requests for materials  
should be addressed to  
J.S. (jingsun@mail.sic.  
ac.cn)

# Three-Dimensional Fe<sub>2</sub>O<sub>3</sub> Nanocubes/ Nitrogen-doped Graphene Aerogels: Nucleation Mechanism and Lithium Storage Properties

Ronghua Wang, Chaohe Xu, Jing Sun &amp; Lian Gao

The State Key Lab of High Performance Ceramics and Superfine Microstructure, Shanghai Institute of Ceramics, Chinese Academy of Sciences, 1295 Ding Xi Road, Shanghai 200050.

We developed a solvothermal-induced self-assembly approach to construct three dimensional (3D) macroscopic Fe<sub>2</sub>O<sub>3</sub> nanocubes/nitrogen-doped graphene (Fe<sub>2</sub>O<sub>3</sub>-NC/GN) aerogel as anode materials for lithium-ion batteries (LIBs). The Fe<sub>2</sub>O<sub>3</sub> nanocubes with length of ~50 nm are homogeneously anchored on 3D GN frameworks and as spacers to separate the neighboring GN sheets. Based on intensively investigations on the early stages of formation process, it is discovered that a non-classical nanoparticle-mediated crystallization process and a subsequent classical ion-mediated growth dominate the nanocube formation. This is totally different from the commonly recognized classical atom-mediated crystallization and ripening mechanism. Benefitting from the unique structures and characteristics, the optimized Fe<sub>2</sub>O<sub>3</sub>-NC/GN aerogel exhibits excellent rate capability, outstanding long-term cyclic stability at high current densities, which are outperforming most of Fe<sub>2</sub>O<sub>3</sub>/GS hybrid electrodes. These results suggest us to in-depth understand the detailed crystallization process, and rational design and precisely control the morphologies of nanocrystals on graphene for high performance energy applications.

Lithium-ion batteries (LIBs) are one of the most promising energy storage devices for upcoming large-scale applications in electric vehicles because of high energy density, long lifespan and environmental benignity<sup>1</sup>. To meet the demands of higher energy density and power density, various transition metal oxides (M<sub>x</sub>O<sub>y</sub>)<sup>2,3</sup>, which possess significantly higher capacities than that of the current commercial anode material (graphite), are widely explored and studied as promising anode materials of LIBs. However, such promise has been hampered by their poor cycling stability and rate performance, which are mainly caused by the drastic volume change during charge/discharge process and low conductivity. Strategies have been proposed to solve these problems by rational designing of diverse nanostructures<sup>4</sup>, and constructing hybrid materials with nanocarbons<sup>5,6</sup>, such as carbon nanotubes or graphene<sup>7-9</sup>.

Graphene, a single layer of carbon atoms arranged in a honeycomb structure with high surface area, fascinating electronic and mechanical properties<sup>10</sup>, has been proved to be an ideal host material for growing and anchoring of functional nanocrystals for high performance lithium ion batteries<sup>11,12</sup>. When hybridized with M<sub>x</sub>O<sub>y</sub> nanocrystals, graphene matrix can facilitate electron transport rate and enhance the chemical activity; and also, the “flexible confinement” function will provide double protections against the aggregation of both components, thus effectively improved the structural stability<sup>5,13</sup>. Until now, various methods, including electrochemical deposition<sup>14</sup>, sol-gel process<sup>15</sup>, hydrothermal or solvothermal method<sup>16</sup>, have been extensively used to synthesize nanocrystals on graphene. However, the state-of-the-art structures are limited to nanoparticles anchored on graphene; more importantly, it remains unexplored and highly desirable to in-depth investigate the nucleation and growth process and rationalize the nanocrystals growth behavior. At present, the commonly recognized nucleation and growth process on the surface of graphene are as follows<sup>17,18</sup>: Firstly, the positively charged metal ions are adsorbed and anchored onto the negatively charged oxygen functional groups on graphene oxide (GO), driven by electrostatic attractive interactions; then metal ions start to hydrolyze and nucleate, followed by a classical atom-mediated crystallization and ripening process to produce the desired graphene-based composites. However, until now, there is no evidence to prove it. Furthermore, it is still an open question that whether other types of nucleation and growth process, such as non-classical (nanoparticle-mediated) crystallization, exists or not in

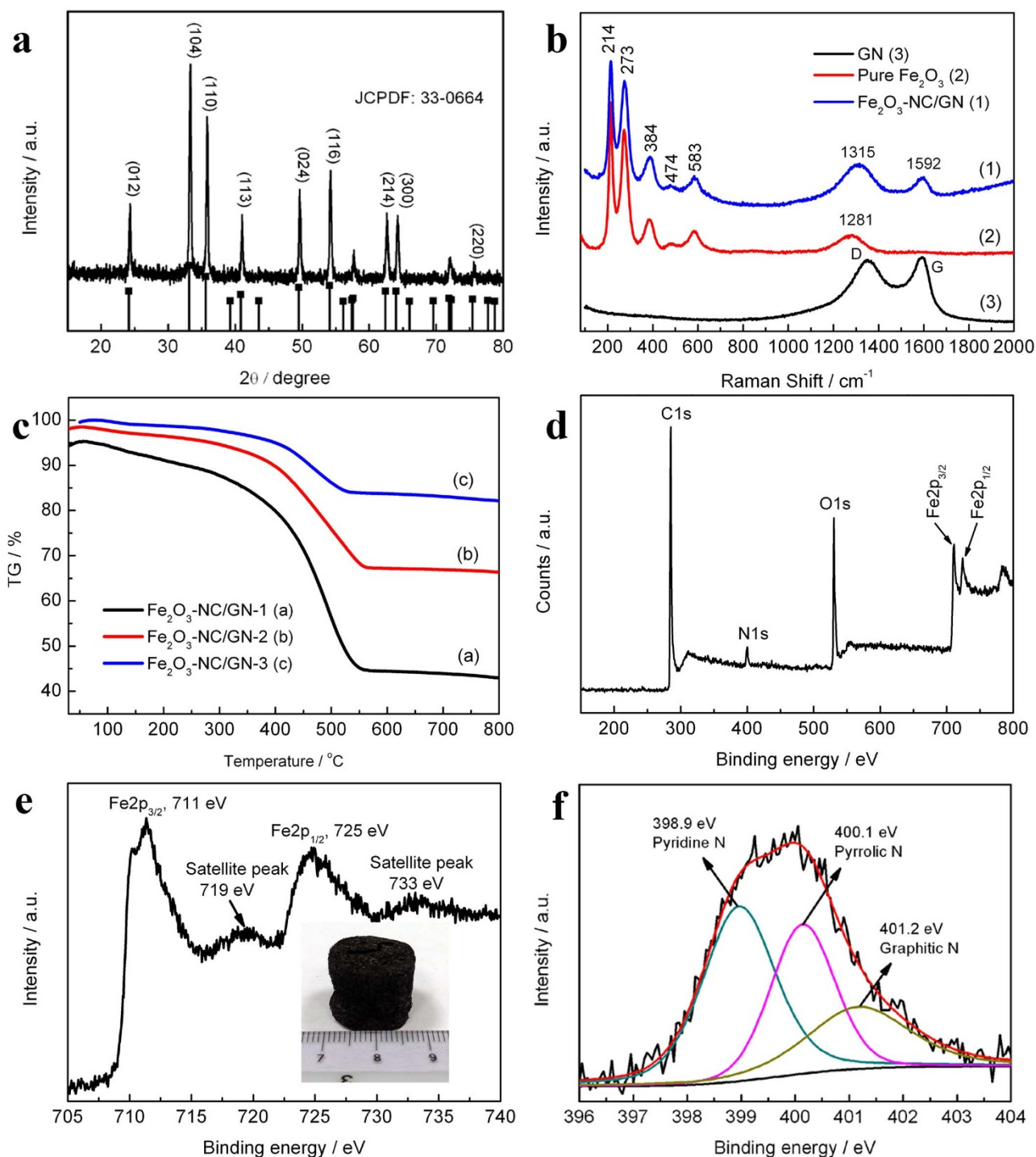


**Figure 1 | Sample characterization:** (a) XRD pattern of  $\text{Fe}_2\text{O}_3\text{-NC/GN-2}$ ; (b) Raman spectra of pure GN,  $\text{Fe}_2\text{O}_3$  and  $\text{Fe}_2\text{O}_3\text{-NC/GN-2}$ ; (c) TG curves  $\text{Fe}_2\text{O}_3\text{-NC/GN}$ ; (d) XPS spectra of  $\text{Fe}_2\text{O}_3\text{-NC/GN-2}$ ; (e) XPS  $\text{Fe}2p$  spectrum; (f) XPS  $\text{N}1s$  spectrum.

the whole process. Therefore, it is of great significance to in-depth understanding of the detailed crystallization process, which will provide the basic guidelines to precisely control the morphologies of nanocrystals on graphene.

Here we report a novel solvothermal-induced self-assembly approach to construct three dimensional (3D) macroscopic  $\text{Fe}_2\text{O}_3$  nanocubes/nitrogen-doped graphene ( $\text{Fe}_2\text{O}_3\text{-NC/GN}$ ) aerogels as anode materials for LIBs. It was discovered that  $\text{Fe}_2\text{O}_3$  nanocubes were obtained through the synergic effect of a non-classical particle-based crystallization process and a subsequent classical ion-mediated growth: A nonclassical particle-based crystallization process, based

on an oriented attachment mechanism and a grain rotation process, yields the initial  $\text{Fe}_2\text{O}_3$  mesocrystals, followed by classical ion-mediated growth to produce the final  $\text{Fe}_2\text{O}_3$  nanocubes. To the best of our knowledge, this is the first time that the non-classical crystallization process of nanocrystals on graphene was discovered and revealed. Previous researches believed that it was quite difficult for nanocrystals to rotate and align freely on graphene or GO due to the strong interface interactions<sup>11,17,18</sup>. So, our result is a new finding for graphene chemistry. Benefitting from the combined N-doped properties and unique characteristics of 3D graphene frameworks, the optimized  $\text{Fe}_2\text{O}_3\text{-NC/GN}$  aerogel exhibits excellent rate capability

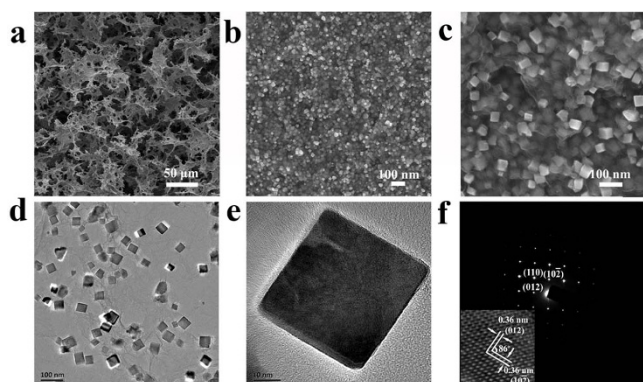


**Figure 2** | (a–c) SEM images of Fe<sub>2</sub>O<sub>3</sub>-NC/GN at different magnification, (d) TEM and (e) HRTEM image of Fe<sub>2</sub>O<sub>3</sub>-NC/GN, (f) the corresponding SAED pattern. The inset in (f) is the enlarged HRTEM image in (e).

(1140, 850, 640 and 420 mA h g<sup>-1</sup> at 200, 1000, 3000, and 6000 mA g<sup>-1</sup>, respectively), outstanding long-term cyclic stability at high current densities (1121 mA h g<sup>-1</sup> after 500 cycles at 500 mA g<sup>-1</sup>), outperforming most of Fe<sub>2</sub>O<sub>3</sub>/GS hybrid electrodes.

## Results

The 3D macroscopic Fe<sub>2</sub>O<sub>3</sub>-NC/GN aerogels were prepared by solvothermal-induced self-assembly process<sup>19</sup>. Specifically, Fe<sup>3+</sup> was first attracted and anchored on GO by electrostatic interactions, then in-situ nucleated and crystallized into Fe<sub>2</sub>O<sub>3</sub> nanocubes. Simultaneously, solvothermal with a DMF solvent highly reduced GO to GN, where DMF acted as both reducing reagent and nitrogen sources<sup>9,20</sup>. Driven by  $\pi-\pi$  stacking interactions, GN anchored with Fe<sub>2</sub>O<sub>3</sub> nanocubes would act as building blocks and self-assemble into 3D monolith hydrogels. After dialysis and freeze-drying, well-defined 3D macroscopic Fe<sub>2</sub>O<sub>3</sub>-NC/GN aerogels can be obtained (inset in Figure 1e).

Figure 1a shows the XRD pattern of Fe<sub>2</sub>O<sub>3</sub>-NC/GN-2, in which all of peaks can be well indexed as rhombohedral  $\alpha$ -Fe<sub>2</sub>O<sub>3</sub> (JCPDS No. 33-0664). Raman spectra shows both the characteristic peaks of graphene and  $\alpha$ -Fe<sub>2</sub>O<sub>3</sub> (A<sub>1g</sub>: 214 and 474 cm<sup>-1</sup>; E<sub>g</sub>: 273, 384 and 583 cm<sup>-1</sup>)<sup>21,22</sup>, further confirming the successful formation of Fe<sub>2</sub>O<sub>3</sub>/GN (Figure 1b). The loading of Fe<sub>2</sub>O<sub>3</sub> on GN can be readily tailored by adjusting the ratio of Fe(NO<sub>3</sub>)<sub>3</sub> to GO during synthesis process. In this study, GN content was varied as 54.5%, 32.1% and 17.7% for Fe<sub>2</sub>O<sub>3</sub>-NC/GN-1, Fe<sub>2</sub>O<sub>3</sub>-NC/GN-2 and Fe<sub>2</sub>O<sub>3</sub>-NC/GN-3, characterized by TG test (Figure 1c), respectively. Hereafter, the detailed characterization was carried out on the optimized sample Fe<sub>2</sub>O<sub>3</sub>-NC/GN-2.

X-ray photoelectron spectroscopy (XPS) measurements were performed to determine the composition of the as-produced Fe<sub>2</sub>O<sub>3</sub>-NC/GN aerogel. The XPS survey spectrum shows predominant C1s peak at 285 eV, N1s peak at ~400 eV, and typical characteristic peaks of Fe<sub>2</sub>O<sub>3</sub> at 711 and 725 eV, corresponding to the Fe2p<sub>3/2</sub> and Fe2p<sub>1/2</sub><sup>16,23</sup>, respectively (Figure 1d, 1e). The Fe2p<sub>3/2</sub> and Fe2p<sub>1/2</sub> main peaks are clearly accompanied by two satellite peaks on their high binding-energy side (at ~8 eV), which are the characteristic peaks of Fe<sub>2</sub>O<sub>3</sub><sup>23</sup>. A high amount of 4.02 at.% nitrogen has been successfully doped into Fe<sub>2</sub>O<sub>3</sub>-NC/GN by the facile solvothermal reaction. The high-resolution N1s spectrum reveals the presence of pyridinic-N (398.9 eV), pyrrolic-N (400.1 eV) and graphitic-N (401.2 eV)<sup>24</sup>, as shown in Figure 1f. Theoretical and experimental investigations demonstrated that nitrogen-doping can decrease the energy barrier of lithium penetration and enhance reactive sites, thereby improve the lithium storage properties compared to pristine graphene<sup>25,26</sup>.

The microstructure of the as-formed 3D macroscopic Fe<sub>2</sub>O<sub>3</sub>-NC/GN aerogel was characterized by SEM and TEM. The SEM image

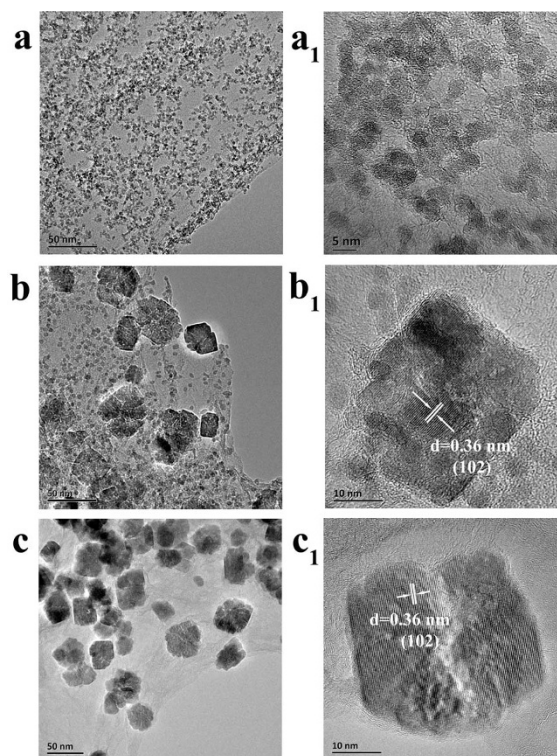


**Figure 3** | TEM images of Fe<sub>2</sub>O<sub>3</sub>-NC/GN obtained at reaction times of 0.5 h (a–a<sub>1</sub>), 1 h (b–b<sub>1</sub>) and 2 h (c–c<sub>1</sub>).

exhibits a well-defined and interconnected 3D porous network of graphene, with continuous macropores in micrometer size (Figure 2a). Close observation reveals Fe<sub>2</sub>O<sub>3</sub> nanocubes, with the edge length of approximately 50 nm, are uniformly anchored on 3D GN frameworks (Figure 2b, 2c). The TEM image further discloses that Fe<sub>2</sub>O<sub>3</sub> nanocubes were highly dispersed and firmly attached on GN, even after the ultrasonication used to disperse Fe<sub>2</sub>O<sub>3</sub>-NC/GN aerogel for characterization (Figure 2d). High-resolution TEM (HRTEM) reveals a typical Fe<sub>2</sub>O<sub>3</sub> nanocube with a single-crystalline nature (Figure 2e). The corresponding SAED pattern further confirms the excellent crystallinity of the as-formed nanocube, with the spots being indexed to (012), (10 $\bar{2}$ ) and (110) of  $\alpha$ -Fe<sub>2</sub>O<sub>3</sub> (Figure 2f). From the magnified HRTEM (inset in Figure 2f), it is found that the crystal lattice fringes have a dihedral angle of 86°, with interplanar distance of ~0.36 nm corresponding to the (012) and (10 $\bar{2}$ ) crystal plane of  $\alpha$ -Fe<sub>2</sub>O<sub>3</sub>. However, Fe<sub>2</sub>O<sub>3</sub> particles (~50 nm) with irregular shapes were obtained without GO added in the above solvothermal system (see supporting information, Figure S1), suggesting the morphology-directing role of GO<sup>13</sup>. Noteworthy, the state-of-the-art structures of 3D hybrid aerogels are limited to nanoparticles anchored on graphene frameworks<sup>9,19,27,28</sup>. To the best of our knowledge, this is the first time that nanocubes/GS hybrid aerogels were constructed. Brunauer-Emmett-Teller (BET) analysis shows that the specific surface area of Fe<sub>2</sub>O<sub>3</sub>-NC/GN-2 reaches up to 231.5 m<sup>2</sup> g<sup>-1</sup> with meso- and macroporous features (Figure S2), exceeding those of other graphene-based aerogels<sup>9,19,27,28</sup>.

To disclose the formation mechanisms of nanocubes, we studied the morphology evolution of Fe<sub>2</sub>O<sub>3</sub> on graphene with different reaction time. Poorly crystallined nanoparticles with size of 2–4 nm were obtained as the first species with a shortened solvothermal time of 0.5 h (Figure 3a–a<sub>1</sub>, S3). HRTEM shows these small nanoparticles are randomly oriented and have a tendency to aggregate together to minimize the overall surface energy of the system<sup>29</sup>. Prolonging solvothermal time to 1 h, the crystallinity of the product significantly enhances (Figure S3). It can observe that many irregular cubic nano-

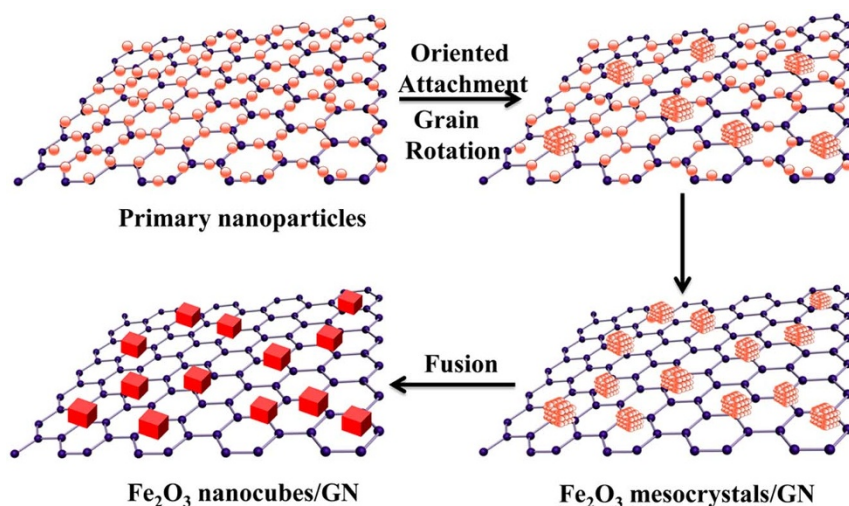


**Figure 4** | Schematic illustration of the formation mechanisms of  $\text{Fe}_2\text{O}_3$  nanocubes from amorphous primary nanoparticles, mesocrystal intermediates to single-crystals.

particles assembled from small nanocrystals start to appear in the typical TEM images, with amorphous nanoparticles remain exist (Figure 3b-b<sub>1</sub>). HRTEM image reveals that these subunits share the same crystallographic orientation with exposed {012} planes, representing monocystal-like lattice fringes. This means the assembly of these subunits is based on an oriented attachment (OA) mechanism<sup>30–32</sup>. Further analysis shows the presence of internal lattice defects and dislocations, which should be a trace of a nonclassical particle-based crystallization process<sup>31,33,34</sup> (Figure S4). The preferred attachment of nanograins with exposed {012} planes is attributed to the fact that the cationic thermal hydrolysis product of DMF ( $\text{NH}_2(\text{CH}_3)_2^+$ ) can adsorb the O-terminated layer of {012} planes, thus stabilize the high-energy {012} planes<sup>29,35</sup>. When the reaction time increased to 2 h, all of primary nanoparticles completely assembled into irregular cubic mesocrystals (Figure 3c). The same crystallographic orientation as well as internal lattice defects further confirms an OA mechanism (Figure S5). Prolonging the reaction time to 6 h, the mesocrystal intermediates gradually crystallographic fuse into imperfect single crystals with more regular cubic shape (Figure 2).

Based on the above time-dependent transformation process, first  $\text{Fe}^{3+}$  was attracted onto oxygen functional groups of GO through electrostatic interactions; then hydrolyzed, nucleated and grew into primary nanoparticles on the surface of GO. To minimize the overall energy of the system, the primary nanoparticles have a tendency to aggregate together<sup>36</sup>. When the reaction time prolonged, at the macroscopic scale, the hydrogel gradually shrunk to a smaller size due to the higher reduction degree of GO<sup>37</sup>. This shrinking process can further facilitate the closer connection between adjacent nanoparticles, and nanoparticles oriented mitigation and moving along graphene. When closely enough, these randomly oriented neighboring nanoparticles are mutually attracted by van der Waals forces, electrostatic interactions, polarization forces and so on<sup>33,38,39</sup>, and will spontaneously rotate to find the lowest-energy configuration<sup>34,40,41</sup>. This results in a coherent grain-grain interface (the grains share the same crystallographic orientation) by eliminating common boundaries, so that adjacent grains oriented attached, coalesce and thereby form larger mesocrystals<sup>30,42,43</sup>. Such grain rotation-induced grain coalescence is frequently observed in the case of colloidal nanocrystals system<sup>34,44</sup>, but is observed for the first time on the surface of graphene in the present work. Previous researches believed that it is quite difficult for nanocrystals to rotate and align freely on graphene or graphene oxide due to the strong interface interactions<sup>17,18</sup>. So, our result is a new finding for graphene chemistry.

Afterwards, due to the crystallographic fusion<sup>29</sup>, the mesocrystal intermediates change into single crystalline nanocubes with many structural defects. Therefore,  $\text{Fe}_2\text{O}_3$  nanocubes are obtained through the synergic effect of oriented attachment and ripening mechanism. Briefly, a nonclassical particle-based crystallization process, based on an oriented attachment mechanism and a grain rotation process, yields the initial  $\text{Fe}_2\text{O}_3$  mesocrystals, followed by classical ion-mediated growth involving face-selective  $\text{NH}_2(\text{CH}_3)_2^+$  adsorption to produce the final  $\text{Fe}_2\text{O}_3$  nanocubes. Based on the above discussion, a reaction mechanism was proposed in Figure 4. The shape evolution of  $\text{Fe}_2\text{O}_3$  nanocubes is valuable for the precise understanding of the formation process of nanocrystals on graphene, which may be applicable for the fine fabrication of other graphene-based hybrid with more novel morphologies.

In the synthesis of mesocrystal intermediate in literature, polymer additives or surfactants were usually needed as a face selective adsorption additive, which assists the crystal growth and self-assembly of nanocrystals into mesocrystals<sup>31,43,45</sup>. Here, the thermal hydrolysis product of DMF ( $\text{NH}_2(\text{CH}_3)_2^+$ ) can successfully act as the structure-directing agent, thus achieving an additive-free synthetic route. On the other hand, DMF also play a key role in realizing the selective and uniform anchoring of  $\text{Fe}_2\text{O}_3$  on GN. When DMF was replaced with  $\text{H}_2\text{O}$ , undefined  $\text{Fe}_2\text{O}_3$  nanoparticles, instead of nanocubes, severely aggregated on GS (Figure S6, S7). This is because the  $\text{H}_2\text{O}$  system will facilitate a higher hydrolysis and condensation velocity of  $\text{Fe}^{3+}$ <sup>19,43,46</sup>. The nucleation process is hard to control, thus resulting in severe agglomeration. However, in DMF, the trace amount of water results in decreasing yet well-controllable hydrolysis and condensation rate<sup>47–49</sup>. Thus, the heterogeneous nucleation of  $\text{Fe}_2\text{O}_3$  on GN can be preferentially achieved, contributing to an ultra-dispersed distribution of  $\text{Fe}_2\text{O}_3$  nanocubes.

## Discussion

The 3D macroscopic  $\text{Fe}_2\text{O}_3$ -NC/GN aerogels, composed of  $\text{Fe}_2\text{O}_3$  nanocubes ultra-dispersed on GN framework, simultaneously possesses high specific surface area, hierarchical porous structure and nitrogen-doping, thus can greatly improve the lithium storage properties. Detailed discussions were carried out on the optimized sample  $\text{Fe}_2\text{O}_3$ -NC/GN-2 (Figure S8). Figure 5a shows the CV curves of  $\text{Fe}_2\text{O}_3$ -NC/GN for the first five cycles. In the first cathodic scan, one well-defined reduction peak can be resolved at  $\sim 0.65$  V, corresponding to the electrochemical reduction reaction of  $\text{Fe}_2\text{O}_3$  accompanying with lithium ion insertion ( $\text{Fe}_2\text{O}_3 + 6\text{Li} + 6\text{e}^- \rightarrow 2\text{Fe} + 3\text{Li}_2\text{O}$ )<sup>50,51</sup>. One anodic peak is also observed at  $\sim 1.75$  V, attributing

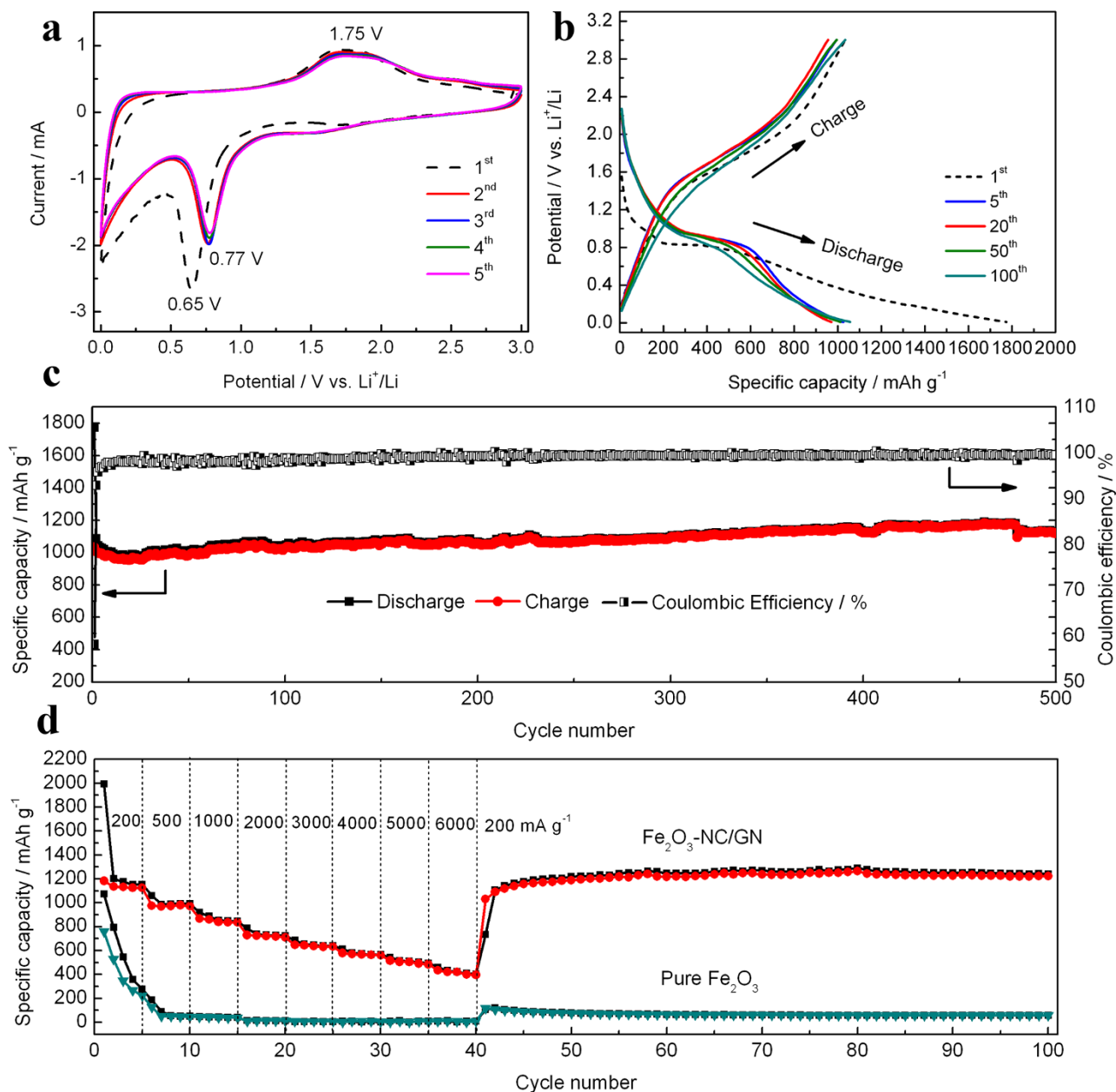


**Figure 5** | (a) Cyclic voltammograms for the first five cycles of  $\text{Fe}_2\text{O}_3\text{-NC/GN}$  electrode; (b) charge-discharge voltage profiles of  $\text{Fe}_2\text{O}_3\text{-NC/GN}$  electrode at a current density of  $500 \text{ mA g}^{-1}$ ; (c) Cycle performance of  $\text{Fe}_2\text{O}_3\text{-NC/GN}$  electrode at a current density of  $500 \text{ mA g}^{-1}$ ; (d) Rate capability of  $\text{Fe}_2\text{O}_3\text{-NC/GN}$  and pure  $\text{Fe}_2\text{O}_3$  at different current densities.

to the reversible oxidation of Fe to  $\text{Fe}_2\text{O}_3$ <sup>52</sup>. In the subsequent cycles, the cathodic peak shifts to  $\sim 0.77 \text{ V}$  while the anodic peak exhibits very slight modification. It is noteworthy that the peak intensity and integral areas are almost identical from the second cycle to the fifth cycle, suggesting the good reversibility and stable performance of the electrode<sup>53,54</sup>. Figure 5b exhibits the discharge/charge profiles of  $\text{Fe}_2\text{O}_3\text{-NC/GN-2}$  at a current density of  $500 \text{ mA g}^{-1}$ , in which a discharge potential plateau at  $\sim 0.9 \text{ V}$  and charge potential plateau at  $\sim 1.8 \text{ V}$  appear, in good agreement with the CV results. Noteworthy, the discharge and charge capacities are as high as  $1774.6$  and  $1033.4 \text{ mAh g}^{-1}$ , respectively, based on the total weight of the composite. Such performance is higher than the theoretical specific capacity of  $\text{Fe}_2\text{O}_3\text{-NC/GN-2}$  ( $C_{\text{theo}} = C_{\text{Fe}_2\text{O}_3, \text{theo}} \times \%_{\text{Fe}_2\text{O}_3} + C_{\text{GN, theo}} \times \%_{\text{GN}} = 1007 \times 67.9\% + 744 \times 32.1\% = 922.6 \text{ mAh g}^{-1}$ ), which may due to the large electrochemical interface lithium storage, superior electrochemical activities and also partial reversible reaction of the SEI<sup>7,8</sup>.

The long-term cycling stability was tested at a high current density of  $500 \text{ mA g}^{-1}$  for 500 cycles (Figure 5c). The capacity slightly decreases during the initial 20 cycles, followed by gradually increasing in the subsequent cycles. A high capacity of  $1121 \text{ mAh g}^{-1}$  is maintained till 500 cycles, corresponding to the capacity retention of 108.5%. This demonstrates an excellent prolonged cycling stability and is quite remarkable compared to the previous results of  $\text{Fe}_2\text{O}_3/\text{graphene}$  electrodes<sup>54–59</sup>. The slight increase of capacity may due to an activation process in electrode material or an improved surface wetting of electrolyte<sup>7,8</sup>. Additionally, the average coulombic efficiency achieved nearly 100% from the second cycle, indicating stabilization of SEI<sup>19</sup>.

The rate capability of the hybrid was further evaluated by charge/discharge at various current densities from 200 to  $6000 \text{ mA g}^{-1}$  (Figure 5d). Our 3D macroscopic  $\text{Fe}_2\text{O}_3\text{-NC/GN}$  hybrid delivers very high capacities of  $1140, 970, 850$  and  $720 \text{ mAh g}^{-1}$  at current densities of 200, 500, 1000 and  $2000 \text{ mA g}^{-1}$ , respectively. Even at ultra-



high current density of 3000, 4000, 5000 and 6000 mA g<sup>-1</sup>, the capacities still reach up to 640, 570, 500 and 420 mAh g<sup>-1</sup>. Importantly, a capacity of 1220 mAh g<sup>-1</sup> can be recovered in another 60 cycles when the current density returns to 200 mA g<sup>-1</sup>, further implying the high reversibility of the electrode. Noteworthy, the rate capability of Fe<sub>2</sub>O<sub>3</sub>-NC/GN outperforms those of reported Fe<sub>2</sub>O<sub>3</sub>/GS aerogels (372 mAh g<sup>-1</sup> under the current density of 5000 mA g<sup>-1</sup>)<sup>59</sup> and most of other Fe<sub>2</sub>O<sub>3</sub> based hybrids<sup>51,60–66</sup> (few of them have reported the rate performance under high current density of 6000 mA g<sup>-1</sup>). The high capacities, outstanding cyclic stability and remarkable rate capability may be due to the synergistic coupling effects in Fe<sub>2</sub>O<sub>3</sub>-NC/GN: On one hand, the small size of Fe<sub>2</sub>O<sub>3</sub> nanocubes can significantly shorten the lithium ion and electron diffusion distance. On the other hand, the porous structure can accommodate volume change of Fe<sub>2</sub>O<sub>3</sub> and favor electrolyte penetration, leading to fast lithium ion transport. Furthermore, the inter-connecting GN network provides 3D electron conducting channels within the electrode.

## Conclusion

In conclusion, we have developed a solvothermal-induced self-assembly approach to construct 3D macroscopic Fe<sub>2</sub>O<sub>3</sub>-NC/GN aerogel as high performance anode materials for LIBs. Well shaped Fe<sub>2</sub>O<sub>3</sub> nanocubes with length of ~50 nm are homogeneously anchored on 3D GN frameworks and separated the neighboring GN sheets. Detail TEM investigation proved that a non-classical nanoparticle-mediated crystallization process and a subsequent classical ion-mediated growth dominated the nanocube formation. We found that primary nanoparticles can diffuse and orient together on graphene to form cube-like Fe<sub>2</sub>O<sub>3</sub> mesocrystals through the oriented attachment (OA) mechanism, perhaps driven by the force of graphene shrinking during 3D macroscopic graphene aerogel formation. In order to decrease the surface energy of nanoparticles, grain rotation and fusion process successive occurred to produce the final single crystalline Fe<sub>2</sub>O<sub>3</sub> nanocubes with structural defects.

The porous-enriched structures of GN and the strong interfacial interaction between Fe<sub>2</sub>O<sub>3</sub> nanocubes and GN are beneficial for efficiently preventing volume expansion/contraction of Fe<sub>2</sub>O<sub>3</sub> and facilitating electrolyte penetration. As a result, such a 3D macroscopic Fe<sub>2</sub>O<sub>3</sub>-NC/GN aerogel exhibits excellent rate capability, outstanding long-term cyclic stability at high current densities. Our results highlighted the importance of in-depth understanding of the crystallization process, and further rational design and precisely control the morphologies of nanocrystals on graphene for high performance energy applications.

## Methods

Graphene oxide (GO) was prepared from graphite powder (Alfa-Aesar) by the modified Hummers method<sup>20</sup>. GO dispersion with a N,N-dimethylformamide (DMF) solvent was obtained by solvent exchange method from the as-exfoliated aqueous GO dispersion<sup>20</sup>. Typically, aqueous GO dispersion was subjected to centrifugation at 11000 rpm for 30 min. The supernatant was removed and GO was re-dispersed in DMF. This process was repeated for more than five times, and finally GO dispersion in DMF was diluted to 2 mg mL<sup>-1</sup>.

The 3D macroscopic Fe<sub>2</sub>O<sub>3</sub>-NC/GN aerogels were prepared by solvothermal-induced self-assembly strategy developed in our group<sup>19</sup> and a subsequent freeze-drying process. Typically, iron nitrate (Fe(NO<sub>3</sub>)<sub>3</sub>·9H<sub>2</sub>O) was first added to GO dispersion in DMF. The mixed dispersion was ultrasonicated for 30 min and then solvothermally treated at 180°C for 6 h to obtain a 3D macroscopic Fe<sub>2</sub>O<sub>3</sub>-NC/GN monolith. Finally, the monolith was washed repeatedly with distilled water, and freeze-dried into an aerogel for further use. To optimize the electrochemical performance, graphene content was varied as 54.5%, 32.1% and 17.7%; named as Fe<sub>2</sub>O<sub>3</sub>-NC/GN-1, Fe<sub>2</sub>O<sub>3</sub>-NC/GN-2 and Fe<sub>2</sub>O<sub>3</sub>-NC/GN-3, respectively. Detailed characterization was carried out on the optimized sample Fe<sub>2</sub>O<sub>3</sub>-NC/GN-2 hereafter.

As a control, pure Fe<sub>2</sub>O<sub>3</sub> without GN were also prepared by solvothermal treating of Fe(NO<sub>3</sub>)<sub>3</sub>·9H<sub>2</sub>O in DMF via a similar procedure. In another experiment, Fe(NO<sub>3</sub>)<sub>3</sub>·9H<sub>2</sub>O was added into GO dispersion in H<sub>2</sub>O, instead of DMF, and was hydrothermally treated at 180°C for 6 h.

**Electrode Preparation.** The electrodes were prepared by mixing 80 wt% active material, 10 wt% conducting carbon black, and 10 wt% polyvinylidene fluoride binder

in N-methyl-2-pyrrolidone. The homogeneous slurries were then pasted on copper current collector and dried under vacuum at 110°C for 12 h. The mass loading was ~1.0 mg cm<sup>-2</sup>.

**Material Characterization.** The morphology was characterized by transmission electron microscope (TEM, JEM-2100F, JEOL, Tokyo, Japan). The field-emission scanning electron microscope (FE-SEM) analysis was performed on JSM-6700F at an acceleration voltage of 10.0 kV. X-ray diffraction (XRD) was carried out on D/max 2550V X-ray diffraction-meter with Cu-Kα irradiation at λ=1.5406. Raman spectroscopy was recorded on a DXR Raman Microscope, Thermal Scientific Corporation, USA, with a 532 nm excitation length. Thermal gravimetric analysis (TGA) was conducted in air at heating rate of 10°C min<sup>-1</sup>. X-ray photoelectron spectroscopy (XPS) analysis was conducted using twin anode gun, Mg Kα (1253.6 eV) (Microlab 310F Scanning Auger Microprobe, VG SCIENTIFIC LTD). N<sub>2</sub> adsorption/desorption isotherms were determined using a Micromeritics ASAP2010 Analyzer (USA).

**Electrochemical Measurements.** Cyclic voltammetry (CV) was carried out in a voltage range of 0–3.0 V with a scan rate of 0.5 mV s<sup>-1</sup>. The electrochemical properties of the electrodes were characterized at room temperature. Li foil was used as the counter electrode. The electrolyte was 1 M LiPF<sub>6</sub> in a 50:50 w/w mixture of ethylene carbonate (EC) and dimethyl carbonate (DMC). Cell assembly was carried out in glove box with the concentrations of moisture and oxygen below 1 ppm. The batteries were measured using a CT2001 battery tester.

1. Arico, A. S., Bruce, P., Scrosati, B., Tarascon, J. M. & Van Schalkwijk, W. Nanostructured materials for advanced energy conversion and storage devices. *Nature Mater.* **4**, 366–377 (2005).
2. Reddy, M. V., Subba Rao, G. V. & Chowdari, B. V. R. Metal Oxides and Oxysalts as Anode Materials for Li Ion Batteries. *Chem. Rev.* **113**, 5364–5457 (2013).
3. Melot, B. C. & Tarascon, J. M. Design and Preparation of Materials for Advanced Electrochemical Storage. *Acc. Chem. Res.* **46**, 1226–1238 (2013).
4. Flaherty, D. W. *et al.* Reactive Ballistic Deposition of Nanostructured Model Materials for Electrochemical Energy Conversion and Storage. *Acc. Chem. Res.* **45**, 434–443 (2011).
5. Xu, C. *et al.* Graphene-based electrodes for electrochemical energy storage. *Energy & Environ. Sci.* **6**, 1388–1414 (2013).
6. Xin, S., Guo, Y. G. & Wan, L. J. Nanocarbon Networks for Advanced Rechargeable Lithium Batteries. *Acc. Chem. Res.* **45**, 1759–1769 (2012).
7. Wang, R., Xu, C., Sun, J., Gao, L. & Lin, C. Flexible free-standing hollow Fe<sub>3</sub>O<sub>4</sub>/graphene hybrid films for lithium-ion batteries. *J. Mater. Chem. A* **1**, 1794–1800 (2013).
8. Wang, R. *et al.* Free-standing and binder-free lithium-ion electrodes based on robust layered assembly of graphene and Co<sub>3</sub>O<sub>4</sub> nanosheets. *Nanoscale* **5**, 6960–6967 (2013).
9. Wang, R., Xu, C., Sun, J., Gao, L. & Yao, H. Solvothermal-Induced 3D Macroscopic SnO<sub>2</sub>/Nitrogen-Doped Graphene Aerogels for High Capacity and Long-Life Lithium Storage. *ACS Appl. Mater. & Interfaces* **6**, 3427–3436 (2014).
10. Zhu, Y. W. *et al.* Graphene and Graphene Oxide: Synthesis, Properties, and Applications. *Adv. Mater.* **22**, 3906–3924 (2010).
11. Liang, Y. Y., Li, Y. G., Wang, H. L. & Dai, H. J. Strongly Coupled Inorganic/Nanocarbon Hybrid Materials for Advanced Electrocatalysis. *J. Am. Chem. Soc.* **135**, 2013–2036 (2013).
12. Han, S., Wu, D., Li, S., Zhang, F. & Feng, X. Porous Graphene Materials for Advanced Electrochemical Energy Storage and Conversion Devices. *Adv. Mater.* **26**, 849–864 (2013).
13. Wang, H. & Dai, H. Strongly coupled inorganic-nano-carbon hybrid materials for energy storage. *Chem. Soc. Rev.* **42**, 3088–3113 (2013).
14. Wu, S. X. *et al.* Electrochemical Deposition of Semiconductor Oxides on Reduced Graphene Oxide-Based Flexible, Transparent, and Conductive Electrodes. *J. Phys. Chem. C* **114**, 11816–11821 (2010).
15. Wu, Z. S. *et al.* Anchoring Hydrated RuO<sub>2</sub> on Graphene Sheets for High-Performance Electrochemical Capacitors. *Adv. Funct. Mater.* **20**, 3595–3602 (2010).
16. Xin, J. *et al.* Fe<sub>2</sub>O<sub>3</sub> xerogel used as the anode material for lithium ion batteries with excellent electrochemical performance. *Chem. Commun.* **48**, 7410–7412 (2012).
17. Wang, H. L., Casalongue, H. S., Liang, Y. Y. & Dai, H. J. Ni(OH)<sub>2</sub> Nanoplates Grown on Graphene as Advanced Electrochemical Pseudocapacitor Materials. *J. Am. Chem. Soc.* **132**, 7472–7477 (2010).
18. Wang, H. L., Robinson, J. T., Diankov, G. & Dai, H. J. Nanocrystal Growth on Graphene with Various Degrees of Oxidation. *J. Am. Chem. Soc.* **132**, 3270–3271 (2010).
19. Wang, R. *et al.* Solvothermal-Induced Self-Assembly of Fe<sub>2</sub>O<sub>3</sub>/GS Aerogels for High Li-Storage and Excellent Stability. *Small* **10**, 2260–2269 (2014).
20. Wang, R. H., Wang, Y., Xu, C. H., Sun, J. & Gao, L. Facile one-step hydrazine-assisted solvothermal synthesis of nitrogen-doped reduced graphene oxide: reduction effect and mechanisms. *Rsc Adv.* **3**, 1194–1200 (2013).
21. Nasibulin, A. G. *et al.* Simple and Rapid Synthesis of α-Fe<sub>2</sub>O<sub>3</sub> Nanowires Under Ambient Conditions. *Nano Res.* **2**, 373–379 (2009).



22. Cherian, C. T., Jayaraman, S., M. V., R. V., Sow, C. H. & B., V. R., C. Electrospun  $\alpha$ - $\text{Fe}_2\text{O}_3$  nanorods as stable, high capacity anode material for Li-ion batteries. *J. Mater. Chem.* **22**, 12198–12204 (2012).
23. Nasibulin, A. *et al.* Simple and rapid synthesis of  $\alpha$ - $\text{Fe}_2\text{O}_3$  nanowires under ambient conditions. *Nano Res.* **2**, 373–379 (2009).
24. Li, Y. *et al.* Nitrogen-Doped Graphene Quantum Dots with Oxygen-Rich Functional Groups. *J. Am. Chem. Soc.* **134**, 15–18 (2011).
25. Reddy, A. L. M. *et al.* Synthesis Of Nitrogen-Doped Graphene Films For Lithium Battery Application. *ACS Nano* **4**, 6337–6342 (2010).
26. Li, Y. F., Zhou, Z. & Wang, L. B. CN(x) nanotubes with pyridineline structures: p-type semiconductors and Li storage materials. *J. Chem. Phys.* **129**, 104703 (2008).
27. Chen, W., Li, S., Chen, C. & Yan, L. Self-Assembly and Embedding of Nanoparticles by In Situ Reduced Graphene for Preparation of a 3D Graphene/Nanoparticle Aerogel. *Adv. Mater.* **23**, 5679–5683 (2011).
28. Wu, Z. S. *et al.* 3D nitrogen-doped graphene aerogel-supported  $\text{Fe}_3\text{O}_4$  nanoparticles as efficient electrocatalysts for the oxygen reduction reaction. *J. Am. Chem. Soc.* **134**, 9082–9085 (2012).
29. Duan, X. *et al.* Facet-induced formation of hematite mesocrystals with improved lithium storage properties. *Chem. Commun.* **48**, 12204–12206 (2012).
30. Stroppa, D. G. *et al.* Anomalous oriented attachment growth behavior on  $\text{SnO}_2$  nanocrystals. *Chem. Commun.* **47**, 3117–3119 (2011).
31. Liang, X. D., Gao, L., Yang, S. W. & Sun, J. Facile Synthesis and Shape Evolution of Single-Crystal Cuprous Oxide. *Adv. Mater.* **21**, 2068–2071 (2009).
32. Da Silva, R. O., Goncalves, R. H., Stroppa, D. G., Ramirez, A. J. & Leite, E. R. Synthesis of recrystallized anatase  $\text{TiO}_2$  mesocrystals with Wulff shape assisted by oriented attachment. *Nanoscale* **3**, 1910–1916 (2011).
33. Niederberger, M. & Colfen, H. Oriented attachment and mesocrystals: Non-classical crystallization mechanisms based on nanoparticle assembly. *Phys. Chem. Chem. Phys.* **8**, 3271–3287 (2006).
34. Fang, J., Ding, B. & Gleiter, H. Mesocrystals: Syntheses in metals and applications. *Chem. Soc. Rev.* **40**, 5347–5360 (2011).
35. Chang, Y., Teo, J. J. & Zeng, H. C. Formation of Colloidal  $\text{CuO}$  Nanocrystallites and Their Spherical Aggregation and Reductive Transformation to Hollow  $\text{Cu}_2\text{O}$  Nanospheres. *Langmuir* **21**, 1074–1079 (2004).
36. Yuwono, V. M., Burrows, N. D., Soltis, J. A. & Penn, R. L. Oriented Aggregation: Formation and Transformation of Mesocrystal Intermediates Revealed. *J. Am. Chem. Soc.* **132**, 2163–2165 (2010).
37. Cong, H. P., Ren, X. C., Wang, P. & Yu, S. H. Macroscopic Multifunctional Graphene-Based Hydrogels and Aerogels by a Metal Ion Induced Self-Assembly Process. *ACS Nano* **6**, 2693–2703 (2012).
38. van Huis, M. A. *et al.* Low-Temperature Nanocrystal Unification through Rotations and Relaxations Probed by in Situ Transmission Electron Microscopy. *Nano Lett.* **8**, 3959–3963 (2008).
39. Ribeiro, C. *et al.* Study of Synthesis Variables in the Nanocrystal Growth Behavior of Tin Oxide Processed by Controlled Hydrolysis. *J. Phys. Chem. B* **108**, 15612–15617 (2004).
40. Moore, L. J., Dear, R. D., Summers, M. D., Dullens, R. P. A. & Ritchie, G. A. D. Direct Observation of Grain Rotation-Induced Grain Coalescence in Two-Dimensional Colloidal Crystals. *Nano Lett.* **10**, 4266–4272 (2010).
41. Fang, J., You, H., Kong, P., Ding, B. & Song, X. Size-dependent structure transformation from amorphous phase to crystal. *Appl. Phys. Lett.* **92**, 143111 (2008).
42. Fang, J., Ding, B. & Song, X. Self-assembly ability of building units in mesocrystal, structural, and morphological transitions in Ag nanostructures growth. *Cryst. Growth Des.* **8**, 3616–3622 (2008).
43. Song, R.-Q. & Cölfen, H. Mesocrystals-Ordered Nanoparticle Superstructures. *Adv. Mater.* **22**, 1301–1330 (2010).
44. Zhang, J. *et al.* Single-Cell Fluorescence Imaging Using Metal Plasmon-Coupled Probe 2: Single-Molecule Counting on Lifetime Image. *Nano Lett.* **8**, 1179–1186 (2008).
45. Zhou, L. & O'Brien, P. Mesocrystals: A New Class of Solid Materials. *Small* **4**, 1566–1574 (2008).
46. Kan, J. & Wang, Y. Large and fast reversible Li-ion storages in  $\text{Fe}_2\text{O}_3$ -graphene sheet-on-sheet sandwich-like nanocomposites. *Sci. Rep.* **3**, 3502 (2013).
47. Wang, H., Robinson, J. T., Diankov, G. & Dai, H. Nanocrystal Growth on Graphene with Various Degrees of Oxidation. *J. Am. Chem. Soc.* **132**, 3270–3271 (2010).
48. Wang, H. L. *et al.*  $\text{LiMn}_{1-x}\text{Fe}_x\text{PO}_4$  Nanorods Grown on Graphene Sheets for Ultrahigh-Rate-Performance Lithium Ion Batteries. *Angew. Chem. Int. Ed.* **50**, 7364–7368 (2011).
49. Wang, H., Casalongue, H. S., Liang, Y. & Dai, H.  $\text{Ni}(\text{OH})_2$  Nanoplates Grown on Graphene as Advanced Electrochemical Pseudocapacitor Materials. *J. Am. Chem. Soc.* **132**, 7472–7477 (2010).
50. Xu, Y. *et al.* Superior electrochemical performance and structure evolution of mesoporous  $\text{Fe}_2\text{O}_3$  anodes for lithium-ion batteries. *Nano Energy* **3**, 26–35 (2014).
51. Yan, Q. Y. *et al.* Hierarchical hollow spheres of  $\text{Fe}_2\text{O}_3$  composed of ultrathin nanosheets for lithium storage and photocatalytic water oxidation. *Energy & Environ. Sci.* **6**, 987–993 (2013).
52. Kim, I. T., Magasinski, A., Jacob, K., Yushin, G. & Tannenbaum, R. Synthesis and electrochemical performance of reduced graphene oxide/maghemite composite anode for lithium ion batteries. *Carbon* **52**, 56–64 (2013).
53. Zhang, L., Wu, H. B. & Lou, X. W. D. Iron-Oxide-Based Advanced Anode Materials for Lithium-Ion Batteries. *Adv. Energy Mater.* **4**, 1300958 (2014).
54. Lin, J. *et al.* Iron Oxide Nanoparticle and Graphene Nanoribbon Composite as an Anode Material for High-Performance Li-Ion Batteries. *Adv. Funct. Mater.* **24**, 2044–2048 (2013).
55. Ruoff, R. S., Zhu, X. J., Zhu, Y. W., Murali, S. & Stollers, M. D. Nanostructured Reduced Graphene Oxide/ $\text{Fe}_2\text{O}_3$  Composite As a High-Performance Anode Material for Lithium Ion Batteries. *ACS Nano* **5**, 3333–3338 (2011).
56. Du, M., Xu, C. H., Sun, J. & Gao, L. One step synthesis of  $\text{Fe}_2\text{O}_3$ /nitrogen-doped graphene composite as anode materials for lithium ion batteries. *Electrochim. Acta* **80**, 302–307 (2012).
57. Du, M., Xu, C. H., Sun, J. & Gao, L. Synthesis of  $\alpha$ - $\text{Fe}_2\text{O}_3$  nanoparticles from  $\text{Fe}(\text{OH})_3$  sol and their composite with reduced graphene oxide for lithium ion batteries. *J. Mater. Chem. A* **1**, 7154–7158 (2013).
58. Yu, S.-H. *et al.* Structure-Properties Relationship in Iron Oxide-Reduced Graphene Oxide Nanostructures for Li-Ion Batteries. *Adv. Funct. Mater.* **23**, 4293–4305 (2013).
59. Xiao, L. *et al.* Self-Assembled  $\text{Fe}_2\text{O}_3$ /Graphene Aerogel with High Lithium Storage Performance. *ACS Appl. Mater. & Interfaces* **5**, 3764–3769 (2013).
60. Han, F. *et al.* Nanoengineered Polypyrrole-Coated  $\text{Fe}_2\text{O}_3$ @C Multifunctional Composites with an Improved Cycle Stability as Lithium-Ion Anodes. *Adv. Funct. Mater.* **23**, 1692–1700 (2012).
61. Zhao, Y., Li, J. X., Ding, Y. H. & Guan, L. H. Single-walled carbon nanohorns coated with  $\text{Fe}_2\text{O}_3$  as a superior anode material for lithium ion batteries. *Chem. Commun.* **47**, 7416–7418 (2011).
62. Zhou, G. M. *et al.* A nanosized  $\text{Fe}_2\text{O}_3$  decorated single-walled carbon nanotube membrane as a high-performance flexible anode for lithium ion batteries. *J. Mater. Chem.* **22**, 17942–17946 (2012).
63. Zhang, M. *et al.* A green and fast strategy for the scalable synthesis of  $\text{Fe}_2\text{O}_3$ /graphene with significantly enhanced Li-ion storage properties. *J. Mater. Chem.* **22**, 3868–3874 (2012).
64. Xu, X. D., Cao, R. G., Jeong, S. & Cho, J. Spindle-like Mesoporous  $\alpha$ - $\text{Fe}_2\text{O}_3$  Anode Material Prepared from MOF Template for High-Rate Lithium Batteries. *Nano Lett.* **12**, 4988–4991 (2012).
65. Chen, D. Z., Quan, H. Y., Jun Fei, L. & Lin, G. One-Pot Synthesis of Hematite@Graphene Core@Shell Nanostructures for Superior Lithium Storage. *Nanoscale* **5**, 9684–9689 (2013).
66. Lei, D. N. *et al.*  $\alpha$ - $\text{Fe}_2\text{O}_3$  nanowall arrays: hydrothermal preparation, growth mechanism and excellent rate performances for lithium ion batteries. *Nanoscale* **4**, 3422–3426 (2012).

## Acknowledgments

This work is supported by the 973 Project (2012CB932303), the National Natural Science Foundation of China (Grant No. 50972153, 51072215, and 51172261).

## Author contributions

R.W., C.X. and J.S. conceived the idea, designed the experiments and analyzed the data. R.W. and C.X. performed the experiments. R.W., C.X., J.S. and L.G. participated in discussing the results and in writing the manuscript. All authors reviewed the manuscript.

## Additional information

Supplementary information accompanies this paper at <http://www.nature.com/scientificreports>

**Competing financial interests:** The authors declare no competing financial interests.

**How to cite this article:** Wang, R., Xu, C., Sun, J. & Gao, L. Three-Dimensional  $\text{Fe}_2\text{O}_3$  Nanocubes/Nitrogen-doped Graphene Aerogels: Nucleation Mechanism and Lithium Storage Properties. *Sci. Rep.* **4**, 7171; DOI:10.1038/srep07171 (2014).



This work is licensed under a Creative Commons Attribution-NonCommercial-NoDerivs 4.0 International License. The images or other third party material in this article are included in the article's Creative Commons license, unless indicated otherwise in the credit line; if the material is not included under the Creative Commons license, users will need to obtain permission from the license holder in order to reproduce the material. To view a copy of this license, visit <http://creativecommons.org/licenses/by-nc-nd/4.0/>